CIVIL ENGINEERING AND GEOMECHANICS SERIES

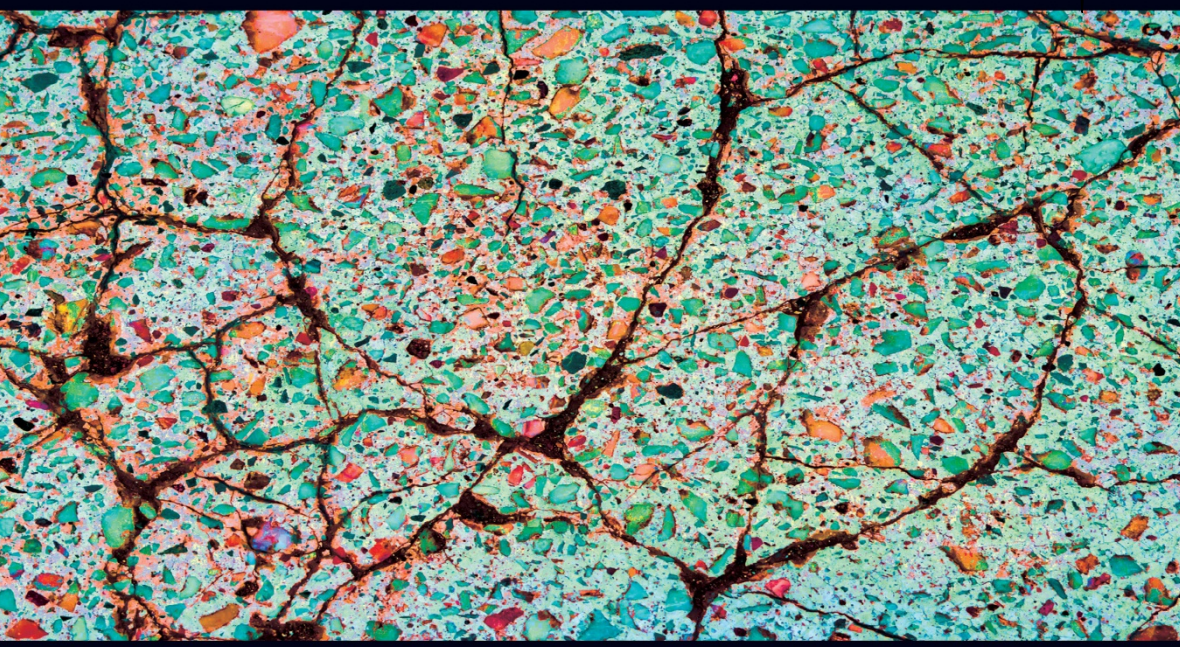

Dynamic Damage and Fragmentation

Edited by
David Edward Lambert
Crystal L. Pasiliao, Benjamin Erzar
Benoit Revil-Baudard
and Oana Cazacu

ISTE WILEY

Dynamic Damage and Fragmentation

Series Editor
Félix Darve

Dynamic Damage and Fragmentation

Edited by

David Edward Lambert
Crystal L. Pasiliao
Benjamin Erzar
Benoit Revil-Baudard
Oana Cazacu

ISTE
WILEY

First published 2019 in Great Britain and the United States by ISTE Ltd and John Wiley & Sons, Inc.

ISTE Ltd
27-37 St George's Road
London SW19 4EU
UK

www.iste.co.uk

John Wiley & Sons, Inc.
111 River Street
Hoboken, NJ 07030
USA

www.wiley.com

Library of Congress Control Number: 2018959945

British Library Cataloguing-in-Publication Data
A CIP record for this book is available from the British Library
ISBN 978-1-78630-408-7

Contents

Preface xiii

Chapter 1. Some Issues Related to the Modeling of Dynamic Shear Localization-assisted Failure 1

Patrice LONGÈRE

1.1. Introduction 1
1.2. Preliminary/fundamental considerations 3
1.2.1. Localization and discontinuity 3
1.2.2. Isothermal versus adiabatic conditions 6
1.2.3. Sources of softening 9
1.2.4. ASB onset 22
1.2.5. Scale postulate 26
1.3. Small-scale postulate-based approaches 27
1.3.1. Material of the band viewed as an extension of the solid material behavior before ASB onset 28
1.3.2. Material of the band viewed as a fluid material 29
1.3.3. ASB viewed as a damage mechanism 31
1.3.4. Assessment 32
1.4. Embedded band-based approaches (large-scale postulate) 33
1.4.1. Variational approaches 34
1.4.2. Enriched finite element kinematics 38
1.4.3. Enriched constitutive model 41
1.4.4. Discussion 43
1.5. Conclusion 44
1.6. Acknowledgments 45
1.7. References 45

Chapter 2. Analysis of the Localization Process Prior to the Fragmentation of a Ring in Dynamic Expansion 53

Skander EL MAÏ, Sébastien MERCIER and Alain MOLINARI

2.1. Introduction 53
2.1.1. Fragmentation experiments 54
2.1.2. Fragmentation theories 54
2.2. An extension of a linear stability analysis developed in [MER 03] . . . 59
2.2.1. Position of the problem. 59
2.2.2. Classical linear stability analysis 60
2.2.3. Evolution of the cross-section perturbation. 62
2.2.4. Analysis of the potential sites of necking. 65
2.3. Outcomes of the approach 70
2.3.1. Effects of the loading velocity on neck spacing distribution 70
2.3.2. Effects of an imposed dominant mode in the initial perturbation 72
2.3.3. Comparison of the approach with numerical simulations 83
2.4. Conclusion 89
2.5. References 90

Chapter 3. Gradient Damage Models Coupled With Plasticity and Their Application to Dynamic Fragmentation 95

Arthur GEROMEL FISCHER and Jean-Jacques MARIGO

3.1. Introduction 95
3.2. Theoretical aspects 96
3.2.1. Gradient damage models. 96
3.2.2. Damage coupled with plasticity 106
3.2.3. Dynamic gradient damage 117
3.3. Numerical implementation 122
3.4. Applications 123
3.4.1. 1D fracture 124
3.4.2. Material behavior 124
3.4.3. Dimensionless parameters 126
3.4.4. 1D period bar 131
3.4.5. Cylinder under internal pressure. 135
3.5. Conclusion 138
3.6. References 139

Chapter 4. Plastic Deformation of Pure Polycrystalline Molybdenum 143

Geremy J. KLEISER, Benoit REVIL-BAUDARD and Oana CAZACU

4.1. Introduction 143
4.2. Quasi-static and dynamic data on a pure polycrystalline Mo 144
4.2.1. Analysis of the quasi-static uniaxial tension test results on smooth specimens 147
4.2.2. Split Hopkinson pressure bar data 154
4.2.3. Taylor cylinder impact data 155
4.3. Constitutive model for polycrystalline Mo 158
4.4. Predictions of the mechanical response 162
4.4.1. FE. predictions of the quasi-static uniaxial tensile response for notched specimens 162
4.5. Conclusions 172
4.6. References 173

Chapter 5. Some Advantages of Advanced Inverse Methods to Identify Viscoplastic and Damage Material Model Parameters 177

Bertrand LANGRAND, Delphine NOTTA-CUVIER, Thomas FOUREST and Eric MARKIEWICZ

5.1. Introduction 177
5.2. Experimental devices for material characterization over a large range of strain rates 180
5.3. Identification of elasto-viscoplastic and damage material Parameters 184
5.3.1. Direct approach for material parameter identification 184
5.3.2. Inverse approaches for material parameter identification. 192
5.4. Conclusions 204
5.5. Acknowledgments 205
5.6. References 205

Chapter 6. Laser Shock Experiments to Investigate Fragmentation at Extreme Strain Rates 213

Thibaut DE RESSÉGUIER, Didier LOISON, Benjamin JODAR, Emilien LESCOUTE, Caroline ROLAND, Loïc SIGNOR and André DRAGON

6.1. Introduction 214
6.2. Phenomenology of laser shock-induced fragmentation 215
6.3. Spall fracture 217

6.4. Microspall after shock-induced melting 222
6.5. Microjetting from geometrical defects 225
6.6. Conclusion 230
6.7. References 231

Chapter 7. One-dimensional Models for Dynamic Fragmentation of Brittle Materials 237

David CERECEDA, Nitin DAPHALAPURKAR and Lori GRAHAM BRADY

7.1. Introduction 237
7.2. Methods 242
7.3. Results 244
7.3.1. Mono-phase materials 244
7.3.2. Multi-phase materials. 251
7.4. Conclusions 258
7.5. References 259

Chapter 8. Damage and Wave Propagation in Brittle Materials . . . 263

Quriaky GOMEZ, Jia LI and Ioan R. IONESCU

8.1. Introduction 263
8.2. Short overview of damage models 264
8.2.1. Effective elasticity of a cracked solid 266
8.2.2. Damage evolution. 268
8.3. 1D wave propagation 275
8.3.1. Problem statement 276
8.3.2. A single family of micro-cracks 278
8.3.3. Three families of micro-cracks 280
8.4. Two-dimensional anti-plane wave propagation 280
8.4.1. Anisotropic damage under isotropic loading 281
8.4.2. Anisotropic loading of an initial isotropic damaged material 284
8.5. Blast impact and damage evolution 286
8.6. Conclusions and perspectives. 291
8.7. Acknowledgments 292
8.8. References 292

Chapter 9. Discrete Element Analysis to Predict Penetration and Perforation of Concrete Targets Struck by Rigid Projectiles 297

Laurent DAUDEVILLE, Andria ANTONIOU, Ahmad OMAR, Philippe MARIN, Serguei POTAPOV and Christophe PONTIROLI

9.1. Introduction 297
9.2. Discrete element model 299
9.2.1. Definition of interactions 299
9.2.2. Constitutive behavior of concrete: Discrete element model 300
9.2.3. Linear elastic constitutive behavior. 301
9.2.4. Nonlinear constitutive behavior. 302
9.2.5. Strain rate dependency. 305
9.3. Simulation of impacts 307
9.3.1. Impact experiments 307
9.3.2. Modeling of impact experiments 308
9.4. Conclusion. 311
9.5. References 311

Chapter 10. Bifurcation Micromechanics in Granular Materials 315

Antoine WAUTIER, Jiaying LIU, François NICOT and Félix DARVE

10.1. Introduction 315
10.2. Application of the second-order work criterion at representative volume element scale 318
10.3. From macro to micro analysis of instability. 322
10.3.1. Local second-order work and contact sliding 322
10.3.2. Role of strong contact network in stable and unstable loading directions 323
10.3.3. From contact sliding to mesoscale mechanisms 326
10.3.4. Micromechanisms leading to bifurcation at the representative volume element scale 329
10.4. Diffuse and localized failure in a unified framework. 331
10.4.1. Diffuse and localized failure pattern 331
10.4.2. Common micromechanisms and microstructures 332
10.5. Conclusion 334
10.6. References 335

Chapter 11. Influence of Specimen Size on the Dynamic Response of Concrete 339

Xu NIE, William F. HEARD and Bradley E. MARTIN

11.1. Introduction 339
11.2. Materials and specimens 341
11.3. Experimental techniques 343
11.3.1. Kolsky compression bar theory and set-up 343
11.3.2. Pulse shaping technique 345
11.4. Results and discussion 350
11.4.1. Pulse shaper design for Kolsky compression bar systems 350
11.4.2. Rate and specimen size effect on failure strength 355
11.5. Conclusion 360
11.6. Acknowledgments 362
11.7. References 362

Chapter 12. Shockless Characterization of Ceramics Using High-Pulsed Power Technologies 365

Jean-Luc ZINSZNER, Benjamin ERZAR and Pascal FORQUIN

12.1. Introduction 365
12.1.1. Presentation of the silicon carbide grades 367
12.2. Principle of the GEPI generator 368
12.3. Dynamic compression of ceramics 370
12.3.1. Lagrangian analysis of velocity profiles 371
12.3.2. Experimental results 372
12.4. Dynamic tensile strength of ceramics 374
12.4.1. Experimental methodology and data processing 375
12.4.2. Characterization of two silicon carbide grades 377
12.4.3. Post-mortem analyses of damaged samples 378
12.5. Conclusions 380
12.6. Acknowledgments 381
12.7. References 381

Chapter 13. A Eulerian Level Set-based Framework for Reactive Meso-scale Analysis of Heterogeneous Energetic Materials 387

Nirmal KUMAR RAI and H.S. UDAYKUMAR

13.1. Introduction 387
13.2. Numerical framework 390
13.2.1. Governing equations 390

13.2.2. Constitutive model for HMX 390
13.2.3. Reactive modeling of HMX 393
13.2.4. Level set representation of embedded interface 395
13.2.5. Image processing approach: Representing real geometries 395
13.3. Results 398
13.3.1. Grid refinement study 400
13.3.2. Collapse behavior of voids present in the pressed HMX material 401
13.3.3. Criticality conditions for Class III and Class V samples 403
13.3.4. Meso-scale criticality conditions for pressed energetic materials 405
13.4. Conclusions 411
13.5. Acknowledgments 412
13.6. References 412

Chapter 14. A Well-posed Hypoelastic Model Derived From a Hyperelastic One 417

Nicolas FAVRIE and Sergey GAVRILYUK

14.1. Introduction 417
14.2. A general hyperelastic model formulation 418
14.3. Evolution equation for the deviatoric part of the stress tensor: neo-Hookean solids 420
14.3.1. Expression of tr(b) as a function of the invariants of S 421
14.3.2. Hypoelastic formulation 423
14.4. Conclusions 424
14.5. Acknowledgments 425
14.6. References 425

Appendix A: Case $a = 0.5$ 429

List of Authors 433

Index 437

Preface

The engineering applications of the Air Force Research Laboratory exercise a diverse spectrum of extreme and dynamic loading conditions that challenges the state-of-the art capability of engineering tools. Munitions applications include the extreme conditions of operational employment as well as the safety protocols designed for protection from accidents and adversarial threats. The operational scenario begins with delivery platforms that can make the systems subject to long-duration ~0 (hrs), high-temperature vibrations and the combination thereof. The engagement phase can induce high-pressure (10s of kbar) mid-duration ~0 (ms) with a combined shear component. The terminal phase of detonation and fragmentation accentuates all of these loadings with ~0 (ns) detonation shock loading reaching Mbar peak pressures all under triaxial stress conditions at strain rates of nearly 0 (106 cm/s/s). The detonation process occurs on the timescale of nanoseconds, with giga watts of power being released in sub-millimeter length scales for shock- and blast-driven work. This seemingly rudimentary, stochastic event has had more than 100 years of research by the broader community, yet significant gaps remain in our understanding.

Furthermore, these systems are built to survive a suite of six hazards mandated via the insensitive munitions (IM) requirements. The IM hazards represent accidents and intentional threats a munition might encounter throughout its life cycle. Each of these also drives the need for constitutive models, including advanced mathematical frameworks for damage, fracture

and fragmentation as well as complementary numerical frameworks, and furthermore, necessary experiments and diagnostics of such.

This book presents recent advances that have been made in the understanding, experimental characterization, theoretical models and numerical simulations of the aforementioned thermo-mechanical processes. It is based on selected invited lectures and lively exchanges of ideas at the 10th US-French symposium "Dynamic damage and fragmentation", Fort Walton Beach, Fl, 17–19 May 2017 organized under the auspices of the International Center for Applied Computational Mechanics (ICACM) at the University of Florida/REEF.

The first part of this book presents an overview of the numerical approaches developed for modeling instabilities leading to plastic flow localization and failure in isotropic metallic materials. For moderate loadings, models for description of strain localization induced by local softening either due to local heating and plastic dissipation (see Chapter 1 on adiabatic shear bands) or due to local damage (see Chapter 3 on gradient plasticity) are presented. With regard to fragmentation of metallic structures, which is a manifestation of local instabilities under extreme environments, the latest developments are presented in Chapter 2. It is demonstrated that linear stability analysis can be successfully used to determine the multiple sites of necking and, furthermore, the fragmentation of a steel ring. While constitutive models and numerical methods are mostly developed assuming isotropic behavior, it should be pointed out that for most materials, the anisotropy in the mechanical response could not be neglected. In Chapter 4, which is devoted to the characterization and modeling of the plastic behavior of refractory metals, it is shown that only by considering the combined influence of anisotropy and strength differential effects on the mechanical response, the particularities of the mechanical response of these materials under extreme environments can be captured with accuracy.

Advancement in understanding and modeling the mechanical behavior can be achieved only through integration with experiments. Recent progress made in the development of methodologies to measure the local strain fields and their direct exploitation to calibrate model parameters using inverse methods are presented in Chapter 5. For extreme loadings, new experimental capabilities that allow us to collect precise and reproducible data are presented in Chapter 6. Specifically, it is shown that laser-driven shocks can

be used to investigate the mechanical response over a range of very high strain rates (~10^7 s^{-1}), high loading pressures, small spatial scales and very short durations of pressure application (~ns). Moreover, their relatively low destructiveness facilitates easier sample recovery and easier instrumentation than the more conventional shock loading techniques based on explosives or plate impacts.

The second part of this book presents an overview of the experimental methods and numerical approaches developed for modeling the overall mechanical behavior and instabilities in brittle materials, including cementitious and ceramic materials and granular media. Such materials are very heterogeneous, and contain a large number of defects such as micro-voids or micro-cracks that strongly influence their quasi-static and dynamic behavior. Chapter 7 presents a one-dimensional model that captures the influence of the local heterogeneity and strain rate on the fragment size probability density functions, while Chapter 8 is devoted to modeling of the influence of the crack density and orientation on three-dimensional wave propagation.

The need to numerically model the limit stage when matter no longer sustain the imparted strains and more or less progressively transits from continuum to a discrete state has led to the development of discrete element methods (DEM). Chapter 9 presents the mathematical foundation of DEM and its application to simulation of a penetration event into a cementitious target, whereas Chapter 10 is devoted to modeling instabilities in this framework.

New experimental capabilities developed in the past decade for studying the high-rate behavior of concrete and ceramics are presented in Chapters 11 and 12.

Finally, another facet of this book is that a variety of materials are presented. As an example, Chapter 13 presents modeling shock-wave phenomena in energetic materials using an Eulerian approach, while Chapter 14 presents an alternative approach to modeling the high-rate regime of behavior using a hypo-elastic modeling approach.

It is a privilege of the Editors to thank all the contributors for their enthusiastic collaboration. Oana Cazacu and Benoit Revil-Baudard gratefully acknowledge the financial support provided by the Office of the Vice-President for Research at the University of Florida, the Doolittle Institute, Niceville, USA, and CEA Gramat, France, for the 10th US-French symposium that enabled the writing of this book.

David Edward LAMBERT, Crystal L. PASILIAO, Benjamin ERZAR,
Benoit REVIL-BAUDARD and Oana CAZACU
October 2018

1

Some Issues Related to the Modeling of Dynamic Shear Localization-assisted Failure

Engineering design of structures to withstand accidental events involving high strain rates and/or impact loading requires predictive modeling capabilities for reproducing numerically potential premature failure following adiabatic shear banding (ASB). The purpose of the present chapter is to review ASB-oriented modeling approaches available in the literature (while not pretending to be exhaustive) that provide a better understanding of ASB and its consequences in structural metals and alloys.

1.1. Introduction

ASB is a mechanism of plastic flow localization known to be triggered by a thermo-mechanical instability in the context of dynamic plasticity (see, for example, Woodward [WOO 90] and Bai and Dodd [BAI 92]). It may be particularly encountered in high-strength metals and alloys including, but not restricted to:

– steels: martensitic steel (Zener and Hollomon [ZEN 44]); HY100 (Marchand and Duffy [MAR 88]); Maraging C300 (Zhou *et al*. [ZHO 96a]); 4340VAR (Minnaar and Zhou [MIN 98]); ARMOX500T (Roux *et al*. [ROU 15]), etc.;

Chapter written by Patrice LONGÈRE.

Dynamic Damage and Fragmentation,
First Edition. Edited by David Edward Lambert, Crystal L. Pasiliao,
Benjamin Erzar, Benoit Revil-Baudard and Oana Cazacu.

– titanium alloys: various titanium alloys (Mazeau *et al*. [MAZ 97]); Ti-6Al-4V (Liao and Duffy [LIA 98]); β-CEZ (Sukumar *et al*. [SUK 13]); UFG pure Ti (Wang *et al*. [WAN 14]), etc.;

– aluminum alloys: AA25XX (Liang *et al*. [LIA 12]); AA50XX (Yan *et al*. [YAN 14]); AA60XX (Adesola *et al*. [ADE 13]); AA70XX (Mondal *et al*. [MON 11]), etc.

Shown as causing either a loss of the ballistic performance of a protection (armor) plate made of high-strength steel and alloys (see, for example, Backman and Goldsmith [BAC 78]) or an increase of the ballistic performance of a kinetic energy penetrator made of depleted uranium, due to the self-sharpening effect (see, for example, Magness and Farrand [MAG 90] and Gsponer [GSP 03]), ASB has been widely studied for defense applications, mostly from a metallurgical viewpoint with the aim to possibly reduce/increase material ASB sensitivity. In parallel, for a long time, a condition for ASB initiation has been considered as a failure criterion in the design of protection structures undergoing impact and other high-strain rate loadings. However, this approach generally leads to over-conservative design since the structure is still able to consume energy in the post-localization stage. ASB is also seen to control chip serration in high-speed machining of, for example, high-strength steel and titanium alloys (see, for example, Molinari *et al*. [MOL 13]), having mitigated effect in the sense that it reduces the cutting force magnitude while generating fluctuations of the cutting force and degrading the surface roughness. Numerically optimizing the cutting conditions implies accounting for ASB.

It has thus become indispensable to explicitly deal with this progressive, irreversible softening mechanism of localized deformation to the same extent as it has become necessary to account for damage-induced softening for related applications.

In this chapter, we present selected ASB-oriented modeling approaches available in the literature (while not pretending to be exhaustive) for guiding researchers and engineers who need to consider and address ASB and its consequences in structural metals and alloys. The inability of standard engineering thermo-viscoplasticity models (see, for example, the Johnson-Cook model) to reproduce ASB-assisted failure (see Batra and Stevens [BAT 98] or Longère *et al*. [LON 09]) has led to the development of enriched models, i.e. models embedding discontinuity either at the constitutive equations level (see Longère *et al*. [LON 03]) or at the FE kinematics level (see, for example, Areias and Belytschko [ARE 07]). There are two

classes of approaches depending on the modeling scale: a first class in which the RVE/FE characteristic length is smaller than the bandwidth, and a second class in which the RVE/FE characteristic length is greater than the bandwidth. RVE stands for the representative volume element for a given material. In the sequel, the former approach is referred to as "small-scale postulate", whereas the latter is referred to as "large-scale postulate" (see Longère *et al*. [LON 18a]). It must be noted that a similar distinction, but with a different nomenclature, can be found in Belytshko *et al*. [BEL 88].

Section 1.2 deals with preliminary considerations and the introduction of basic concepts. Sections 1.3 and 1.4 present some models based on the "small-scale postulate" and "large-scale postulate", respectively. The summary and conclusions are given in section 1.5.

1.2. Preliminary/fundamental considerations

The present work focuses on metals and alloys, even though most of the considerations and concepts presented in the following apply to a wider class of solid materials, including, for example, polymers (below glass transition). In addition, the numerical approach considered for the resolution of the initial boundary value problems involving structural materials susceptible to ASB is here restricted to the finite-element method, which is the most widely used method for engineering applications. Thus, there is a connection between the volume element and the integration point.

1.2.1. *Localization and discontinuity*

First, definitions of basic concepts are introduced:

Discontinuity

It should be recalled that according to the discontinuity theory (see Figure 1.1):

– a "strong" discontinuity involves a discontinuity of the displacement/velocity field;

– a "weak" discontinuity involves a discontinuity of the gradient of the displacement/velocity field, i.e. of the strain/strain rate field.

For example, a crack generates a strong discontinuity, whereas strain localization produces a weak discontinuity. An ASB exhibiting a width with distinct boundaries is thus associated with strain localization involving a weak discontinuity, i.e. a discontinuity of the gradient of displacement/velocity field.

Strain localization

– the "physical" strain localization, as observed experimentally, results from a thermo-mechanical instability due to, for example, thermal softening, damage, microstructural changes or their combination;

– the "numerical" strain localization, as observed in numerical simulations, is characterized by the formation of a band whose width covers only a single (standard) finite element and results from the loss of uniqueness of the solution of the initial boundary value problem (IBVP) in the softening regime, having, as a result, mesh size and orientation dependence of the numerical results.

Ideally, the numerical strain localization would/should numerically reproduce the physical strain localization. However, it is rarely, actually scarcely ever, the case.

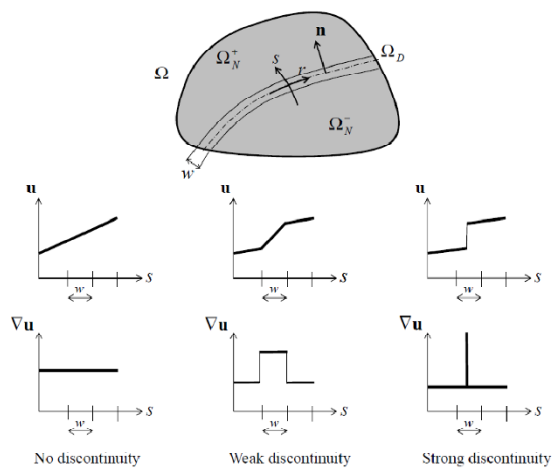

Figure 1.1. *Displacement and strain fields in the absence of discontinuity and in the presence of weak and strong discontinuities. Body Ω with a discontinuity; w represents the discontinuity width and u and ∇u are the displacement/velocity and displacement/velocity gradient, respectively. Source: Longère [LON 18a]*

Based on the well-known experimental results obtained by Marchand and Duffy [MAR 88] on dynamic torsion loading of a thin-walled cylinder made of high-strength steel (see also Roux *et al*. [ROU 15] for impact loading), the following scenario is well established nowadays. During the shear loading of a viscoplastic material, we can distinguish three stages: a first stage of homogeneous deformation, a second stage of weakly heterogeneous deformation and a third stage of strongly heterogeneous deformation. It is during the third stage that ASB occurs and further develops, sometimes leading (see, for example, Longère and Dragon [LON 15] for titanium alloys) to void growth-induced damage and ultimately to fracture in the band wake. Thus, two characteristic lengths are involved: a large one W for weakly heterogeneous deformation and a small one w for strongly heterogeneous deformation (see Figure 1.2).

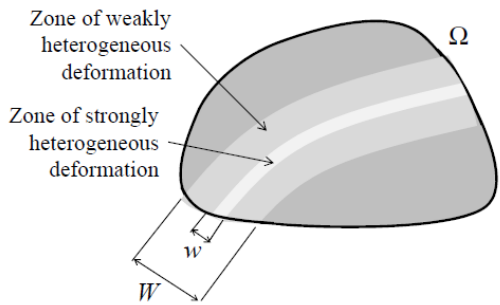

Figure 1.2. *Zones of weakly and strongly heterogeneous deformations according to Marchand and Duffy's terminology [MAR 88]. Source: Longère [LON 18a]*

The non-local modeling framework has been specifically developed to respond to the need for incorporation of material length-scale measures in the constitutive description involving deformation process strongly affected by the presence of material or geometrical imperfections, distribution of defects and strain localization phenomena. A systematic design of the non-local gradient-enhanced continuum model for solving high-velocity impact-related problems has been attempted by Voyiadjis and co-workers. A thermo-viscoplastic and thermo-viscodamage model in this context was introduced by Abu Al-Rub and Voyiadjis [ABU 06a, ABU 06b] and further applied by Voyiadjis *et al*. [VOY 13]. Second-order gradients in the hardening variables and in the damage variable are introduced, and the coupling between these variables and their gradients are accounted for. The proposed theory leads to

numerous material parameters/constants to be determined. They are difficult to be established as based on the limited set of micromechanical gradient-dominated experiments (micro-torsion, micro-indentation, etc.). One of the dominant aspects of non-local gradient-dependent models is performing regularization with respect to discontinuities. Thus, the corresponding length-scale-related variables act as localization limiters. There is a notable affinity between non-local gradient-enhanced modeling and phase field approaches (see, for example, Miehe *et al*. [MIE 16]). An in-depth discussion of non-local models is beyond the scope of this chapter.

The susceptibility of a material to shear banding is characterized by its susceptibility to develop a strongly heterogeneous deformation (involving a small characteristic length, w) from a weakly heterogeneous deformation (involving a large characteristic length, W). Indeed, regardless of the ductile material under consideration, the compression of a cylinder systematically leads to a weakly heterogeneous deformation along the maximum shearing planes (forming cones opposed by their peaks), even under low strain rate, but the weakly heterogeneous deformation will only lead to strongly heterogeneous deformation for materials susceptible to ASB, mostly under high strain rate.

1.2.2. *Isothermal versus adiabatic conditions*

The local form of the heat equation reads

$$\rho c\dot{T} - \lambda\nabla^2 T = \dot{Q}\,;\ \lambda = k\rho c \qquad [1.1]$$

where ρ represents the mass density, c is the specific heat, λ is the thermal conductivity, k is the thermal diffusivity (see Figure 1.3 for values of k for several solid materials), ∇ is the gradient operator, T is the absolute temperature and Q is the rate of heat generation. From equation [1.1], we can derive the thermal diffusion time, associated with the time required for the material to propagate a temperature gradient along a distance L separating the heat source from the heat sink:

$$t_{dif} = \frac{L^2}{2k} \qquad [1.2]$$

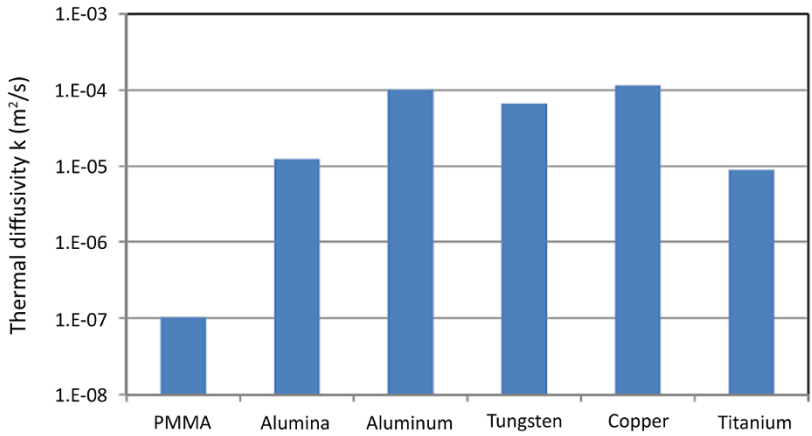

Figure 1.3. *Values of thermal diffusivity k for different solid materials*

Considering a specimen of initial length $\overline{h}_0$ and current length $\overline{h}$ submitted to a compression loading between platens (considered as heat sink), the test time or time needed to reach the strain $\Delta\varepsilon$ is given by

$$t_{test} = \frac{\Delta\varepsilon}{\dot{\varepsilon}} \; ; \; \Delta\varepsilon = \ln\left(\frac{\overline{h}}{\overline{h}_0}\right) = \ln(1+e) ; \; \overline{h} = \overline{h}_0 \exp(\Delta\varepsilon) \qquad [1.3]$$

According to Arruda *et al.* [ARR 95], assuming that the heat source is located in the middle of the specimen (i.e. $L_0 = \overline{h}_0 / 2$ and $L = \overline{h} / 2$), it is possible to compare the test time with the thermal diffusion time using equations [1.2] and [1.3] via the ratio

$$\eta = \frac{t_{test}}{t_{dif}} = \frac{2k}{\left(\overline{h} / 2\right)^2} \frac{\Delta\varepsilon}{\dot{\varepsilon}} = \frac{8k}{\left[\overline{h}_0 \exp(\Delta\varepsilon)\right]^2} \frac{\Delta\varepsilon}{\dot{\varepsilon}} \qquad [1.4]$$

which makes it possible to distinguish isothermal conditions for $\eta >> 1$, adiabatic conditions for $\eta << 1$ and coupled conditions for $\eta \approx 1$.

Now, we can roughly estimate a critical value for the strain rate $\dot{\varepsilon}$ at the transition between isothermal and adiabatic conditions

$$\eta_c = 1 \rightarrow \dot{\varepsilon}_c = 2k \frac{\Delta\varepsilon}{\left[L_0 \exp(\Delta\varepsilon)\right]^2} \qquad [1.5]$$

Critical strain rate $\dot{\varepsilon}_c$ coarse estimates are reported in Figure 1.4 for different materials and for a given specimen characteristic length L_0. According to equation [1.5], the critical strain rate $\dot{\varepsilon}_c$ is directly proportional to the thermal diffusivity *k*: the lower the thermal diffusivity *k*, the lower the critical strain rate $\dot{\varepsilon}_c$. In particular, if aluminum is taken as reference, its critical strain rate is of the same magnitude as tungsten and copper, 10 times higher than that of alumina and titanium and 1,000 times higher than that of PMMA. It should also be noted that the critical strain rate is dependent on the specimen length, in addition to being dependent on the boundary conditions.

Oussouaddi and Klepaczko [OUS 91] and Rusinek *et al.* [RUS 02] conducted numerical simulations in torsion and shear, respectively, considering specific boundary conditions and thermo-viscoplastic constitutive models, in order to estimate the transition from isothermal to adiabatic conditions as a function of strain rate. It is shown that adiabatic conditions can be assumed for copper, aluminum and steel when the strain rate exceeds 10^2 s^{-1} and that increasing the specimen length results in a decrease of the critical strain rate, which is consistent with equation [1.5].

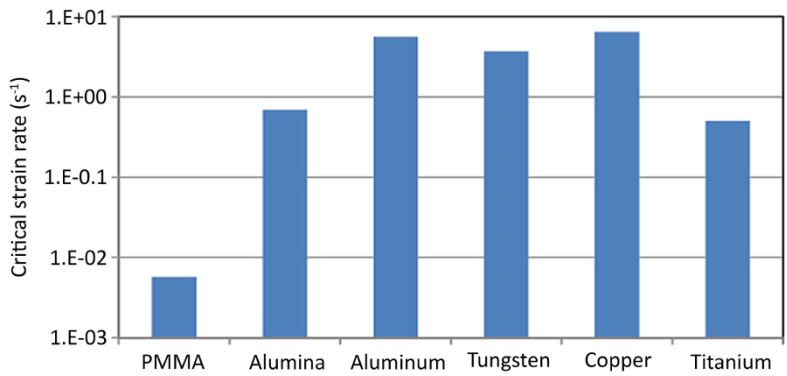

Figure 1.4. *Values of the critical strain rate $\dot{\varepsilon}_c$ for different solid materials; h_0 = 20 mm and e = −50%*

When the strain rate is sufficiently high, implying a very small value for η in equation [1.4], adiabatic conditions can be assumed and the local form of the heat equation [1.1] reduces to

$$\rho c\dot{T} = \dot{Q} \qquad [1.6]$$

1.2.3. *Sources of softening*

As instability leading to the development of ASB results from the competition between hardening and softening mechanisms, here we consider three main sources of softening, namely thermal softening, microstructural changes and micro-damage.

For this aim, here we consider solid materials for which the state potential per unit volume is of the form $\varpi\left(T,\varepsilon^e,\kappa\right)$. Moreover, it is assumed that this potential can be written as the sum of reversible, stored and purely thermal contributions, namely $\varpi^e\left(T,\varepsilon^e\right)$, $\varpi^p\left(T,\kappa\right)$ and $\varpi^T\left(T\right)$

$$\varpi\left(T,\varepsilon^e,\kappa\right)=\varpi^e\left(T,\varepsilon^e\right)+\varpi^p\left(T,\kappa\right)+\varpi^T\left(T\right) \qquad [1.7]$$

where ε^e is the elastic strain tensor and κ is an isotropic hardening variable, generally taken to be the accumulated plastic strain.

The Clausius–Duhem inequality implies that the Cauchy stress tensor σ and the strain hardening force R are expressed as

$$\begin{cases}\sigma\left(\varepsilon^e,T\right)=\dfrac{\partial\varpi\left(T,\varepsilon^e,\kappa\right)}{\partial\varepsilon^e}=\dfrac{\partial\varpi^e\left(T,\varepsilon^e\right)}{\partial\varepsilon^e}\\ R\left(\kappa,T\right)=\dfrac{\partial\varpi\left(T,\varepsilon^e,\kappa\right)}{\partial\kappa}=\dfrac{\partial\varpi^p\left(T,\kappa\right)}{\partial\kappa}\end{cases} \qquad [1.8]$$

Viscoplastic behavior modeled using the overstress concept and yielding according to von Mises is generally assumed, i.e. the yield function is of the form

$$F\left(\sigma,\sigma_y\right)=\sigma_{eq}\left(\sigma\right)-\sigma_y\left(R\left(T,\kappa\right),\kappa,T\right)=\sigma_V\left(\kappa,\dot{\kappa},T\right)\geq 0 \qquad [1.9]$$

where σ_{eq} represents the Mises equivalent stress, $\sigma_y\left(R\left(\kappa,T\right),\kappa,T\right)$ is the rate-independent contribution to the yield stress and $\sigma_V\left(\kappa,\dot{\kappa},T\right)$ is the viscous stress or strain rate-induced overstress, or equivalently

$$\begin{cases}\sigma_{eq}\left(\sigma\right)=\bar{\sigma}_y\left(\kappa,\dot{\kappa},T\right)\\ \bar{\sigma}_y\left(\kappa,\dot{\kappa},T\right)=\sigma_y\left(R\left(T,\kappa\right),\kappa,T\right)+\sigma_V\left(\kappa,\dot{\kappa},T\right)\end{cases} \quad [1.10]$$

where $\bar{\sigma}_y\left(\kappa,\dot{\kappa},T\right)$ can be viewed as a rate-dependent yield stress. Some examples of widely used, engineering-oriented and temperature- and rate-dependent hardening laws are given as follows:

– Johnson–Cook temperature- and rate-dependent model

$$\bar{\sigma}_y\left(\kappa,\dot{\kappa},T\right)=\left(A+B\kappa^n\right)\left(1+C\ln\frac{\dot{\kappa}}{\dot{\kappa}_0}\right)\left(1-\overline{T}^m\right);\ \overline{T}=\frac{T-T_0}{T_m-T_0} \quad [1.11]$$

– Cowper–Symonds rate-dependent model

$$\bar{\sigma}_y\left(\kappa,\dot{\kappa},T\right)=\sigma_y\left(R\left(T,\kappa\right),\kappa,T\right)\left[1+\left(\frac{\dot{\kappa}}{\dot{\kappa}_0}\right)^{1/m}\right] \quad [1.12]$$

– Norton rate-dependent model

$$\sigma_V\left(\dot{\kappa},T\right)=Z\left(T\right)\dot{\kappa}^{1/m(T)} \quad [1.13]$$

where *A, B, C* and *m* are material parameters.

According to the normality rule, the instantaneous plastic strain rate tensor $\mathbf{d}^p$ and the isotropic hardening variable rate $\dot{\kappa}$ read

$$\mathbf{d}^p=\frac{3}{2}\dot{\kappa}\frac{\mathbf{s}}{\sigma_{eq}};\ \dot{\kappa}=\sqrt{\frac{2}{3}\mathbf{d}^p:\mathbf{d}^p}\geq 0;\ \kappa=\int_t\dot{\kappa}dt\geq 0 \quad [1.14]$$

where $\mathbf{s}$ is the deviatoric part of the stress tensor σ.

– **Thermal softening**

The rate of heat generation $\dot{Q}$ in equation [1.1] may be decomposed as

$$\dot{Q}=D+\dot{W}_{TE}+\dot{W}_{TP}+\dot{Q}^h \quad [1.15]$$

where D, $\dot{W}_{TE}$, $\dot{W}_{TP}$ and $\dot{Q}^h$ represent the intrinsic dissipation, the rate of heat exchange due to thermo-elasticity coupling, the rate of heat exchange due to thermo-plasticity coupling and the latent heat involved during, for example, phase transformation, respectively.

The intrinsic dissipation D in [1.12] is by definition the difference between the plastic work rate $\dot{W}_P$ and the stored energy rate $\dot{W}_S$:

$$D = \dot{W}_P - \dot{W}_S \geq 0 \qquad [1.16]$$

The rates of heat exchange due to thermo-elasticity and thermo-plasticity coupling read

$$\begin{cases} \dot{W}_{TE} = T\dfrac{\partial^2 \varpi\left(T, \boldsymbol{\varepsilon}^e, \kappa\right)}{\partial \boldsymbol{\varepsilon}^e \partial T} : \mathbf{d}^e = T\dfrac{\partial^2 \varpi^e\left(T, \boldsymbol{\varepsilon}^e\right)}{\partial \boldsymbol{\varepsilon}^e \partial T} : \mathbf{d}^e = T\dfrac{\partial \boldsymbol{\sigma}\left(T, \boldsymbol{\varepsilon}^e\right)}{\partial T} : \mathbf{d}^e \\ \dot{W}_{TP} = T\dfrac{\partial^2 \varpi\left(T, \boldsymbol{\varepsilon}^e, \kappa\right)}{\partial \kappa \partial T}\dot{\kappa} = T\dfrac{\partial^2 \varpi^p\left(T, \kappa\right)}{\partial \kappa \partial T}\dot{\kappa} = T\dfrac{\partial R\left(T, \kappa\right)}{\partial T}\dot{\kappa} \end{cases} \qquad [1.17]$$

where $\mathbf{d}^e$ represents the elastic strain rate tensor and $\mathbf{a} : \mathbf{b} = c$ is the double scalar product (double contraction). For example, if the reversible and stored contributions of the state potential in [1.7] read

$$\varpi^e\left(T, \boldsymbol{\varepsilon}^e\right) = \frac{1}{2}\boldsymbol{\varepsilon}^e : \mathbf{C}\left(T\right) : \boldsymbol{\varepsilon}^e \ ; \ \varpi^p\left(T, \kappa\right) = h\left(\kappa\right) g\left(T\right) \qquad [1.18]$$

then the Cauchy stress tensor and the strain hardening force and their temperature derivatives take the forms

$$\begin{cases} \boldsymbol{\sigma}\left(T, \boldsymbol{\varepsilon}^e\right) = \mathbf{C}\left(T\right) : \boldsymbol{\varepsilon}^e \\ \boldsymbol{\sigma}_{,T}\left(T, \boldsymbol{\varepsilon}^e\right) = \dfrac{\partial \boldsymbol{\sigma}\left(T, \boldsymbol{\varepsilon}^e\right)}{\partial T} = \mathbf{C}'\left(T\right) : \boldsymbol{\varepsilon}^e \\ R\left(T, \kappa\right) = h'\left(\kappa\right) g\left(T\right) \\ R_{,T}\left(T, \kappa\right) = \dfrac{\partial R\left(T, \kappa\right)}{\partial T} = h'\left(\kappa\right) g'\left(T\right) \end{cases} \qquad [1.19]$$

It must be noted that $\dot{W}_{TE}$ in equation [1.17] is positive in tension and negative in compression; $\dot{W}_{TP}$ in equation [1.17] is generally negative and $\dot{Q}^h$ in equation [1.15] is positive for exothermal transformation and negative for endothermal transformation.

We can rewrite [1.7] as

$$\dot{Q} = \dot{Q}^e + \dot{Q}^p + \dot{Q}^h \qquad [1.20]$$

where

$$\begin{cases} \dot{Q}^e = \dot{W}_{TE} = T\boldsymbol{\sigma}_{,T}\left(T, \boldsymbol{\varepsilon}^e\right) : \mathbf{d}^e \\ \dot{Q}^p = D + \dot{W}_{TP} = \dot{W}_P - \dot{W}_S + \dot{W}_{TP} = \left[\sigma_{eq} - R\left(T,\kappa\right) + T\,R_{,T}\left(T,\kappa\right)\right]\dot{\kappa} \end{cases} \qquad [1.21]$$

We are now introducing the inelastic heat fraction, or the Taylor–Quinney coefficient (see Taylor and Quinney [TAY 34]), β defined as

$$\dot{Q} = \beta \dot{W}_P \qquad [1.22]$$

Substituting equation [1.20] into equation [1.22] leads to

$$\beta = \frac{\dot{Q}}{\dot{W}_P} = \frac{\dot{Q}^e + \dot{Q}^p + \dot{Q}^h}{\dot{W}_P} \qquad [1.23]$$

Using equation [1.21], equation [1.23] becomes

$$\beta = 1 - \frac{\dot{W}_S - \left(\dot{W}_{TE} + \dot{W}_{TP} + \dot{Q}^h\right)}{\dot{W}_P} \qquad [1.24]$$

where $\dot{W}_P$ is positive in the hardening regime and negative in the softening regime. In the absence of latent heat $\dot{Q}^h$, the inelastic heat fraction reduces to

$$\beta = 1 - \frac{\dot{W}_S - \left(\dot{W}_{TE} + \dot{W}_{TP}\right)}{\dot{W}_P} \qquad [1.25]$$